

GaussianHead: High-fidelity Head Avatars with Learnable Gaussian Derivation

Jie Wang, Jiu-Cheng Xie, Xianyan Li, Feng Xu, Chi-Man Pun, and Hao Gao

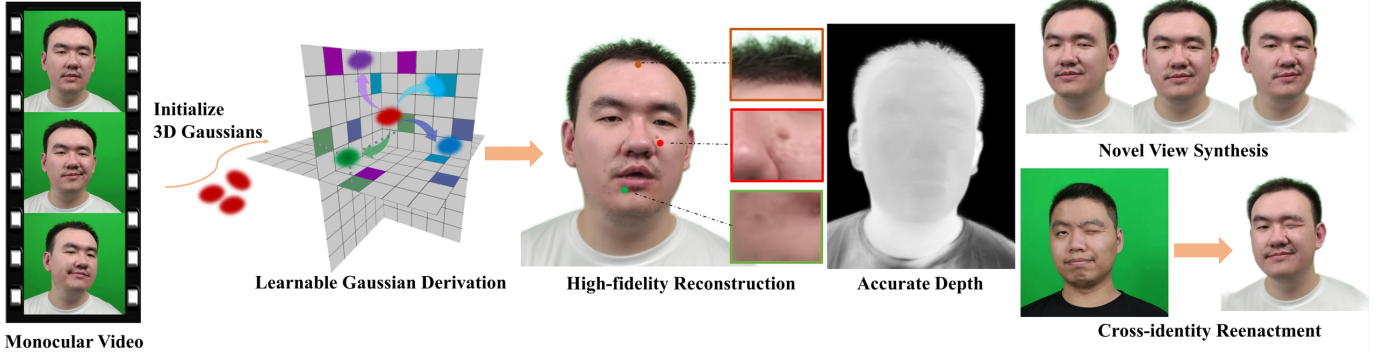


Fig. 1: Based on anisotropic 3D Gaussians and the learnable derivation strategies, our method learns an identity-specific head avatar from a monocular video of the corresponding subject. The proposed GaussianHead demonstrates outstanding performance in self-reconstruction, cross-identity reenactment, and novel-view synthesis tasks.

Abstract—Creating lifelike 3D head avatars and generating compelling animations for diverse subjects remain challenging in computer vision. This paper presents GaussianHead, which models the active head based on anisotropic 3D Gaussians. Our method integrates a motion deformation field and a single-resolution tri-plane to capture the head’s intricate dynamics and detailed texture. Notably, we introduce a customized derivation scheme for each 3D Gaussian, facilitating the generation of multiple “doppelgangers” through learnable parameters for precise position transformation. This approach enables efficient representation of diverse Gaussian attributes and ensures their precision. Additionally, we propose an inherited derivation strategy for newly added Gaussians to expedite training. Extensive experiments demonstrate GaussianHead’s efficacy, achieving high-fidelity visual results with a remarkably compact model size (≈ 12 MB). Our method outperforms state-of-the-art alternatives in tasks such as reconstruction, cross-identity reenactment, and novel view synthesis. The source code is available at: <https://github.com/chiehwangs/gaussian-head>.

Index Terms—Head avatar, 3D gaussian splatting, 3D reconstruction, hybrid neural network.

I. INTRODUCTION

CREATING personalized head avatars is very useful in wide-ranging applications like virtual reality, remote meetings, movies, and games. Previous works usually rely

on synchronized multi-view images of heads to reconstruct photorealistic 3D avatars [1]–[3]. The harsh capturing requirement hinders the wide range of popularity of these techniques among the public. An emergent exploration in this field focuses on using monocular videos to build personalized head avatars, which is much more convenient. Since almost all daily used smartphones now integrate high-quality cameras, this kind of technique has the potential to be used by all end users and may establish more applications like social communication and short video sharing. Nevertheless, the variable geometry and complex appearance of human heads make it very challenging to achieve precise modeling from single-view captures.

Early methods in this direction predominantly rely on pre-trained parametric models [4]–[6] to create coarse facial geometry [7] and corresponding appearance [8]. While limited in fine details, these methods lay a solid foundation for accurate facial motion capture. Building implicit head avatars using Signed Distance Fields (SDF) [9], [10] helps overcome the deficiencies of parametric models and achieve better head geometry [11], [12]. Nevertheless, implicit surfaces lack enough expressive power for fine structures and suffer from inefficient rendering. To this end, combining structured data containers and volume rendering to build volumetric neural radiance fields gradually becomes the current mainstream practice. When it comes to the scope of head construction, Several methods [13], [14] utilize multi-resolution neural voxels as facial expression bases, combining them with expression parameters to produce visually compelling dynamic head avatars. Other approaches [15]–[17] leverage the tri-plane for feature storage, which produces impressive rendering effects and further reduces the quantity of model parameters [18], [19].

Jie Wang, Jiu-Cheng Xie, Xianyan Li and Hao Gao are with the School of Automation and the School of Artificial Intelligence, Nanjing University of Posts and Telecommunications, Nanjing, 210023, China. E-mail: chieh.wangs@gmail.com, jiuchengxie@gmail.com, 9745981xy@gmail.com, tsgaohao@gmail.com.

Feng Xu is with the School of Software and BNRist, Tsinghua University, Beijing 100084, China. E-mail: xufeng2003@gmail.com.

Chi-Man Pun is with the Department of Computer and Information Science, University of Macau, Taipa, Macau. E-mail: cmpun@um.edu.mo.

Jiu-Cheng Xie and Hao Gao are the corresponding authors.

Despite the advantages of tri-plane-formed feature containers, their reliance on a multi-resolution mechanism leaves room for further optimization of the model size. Moreover, the widely adopted axis-aligned mapping is unsuitable in at least two scenarios listed follow. The first case is when multiple primitives are close (the orange and blue blocks in Fig. 2), their projections on each feature plane will be also near. For ease of computation and data saving, each plane is regarded as a grid composed of cells in practice. If these projected positions fall within a single cell, the feature from that single cell will be used to represent information about different primitives, which should be avoided in the pursuit of distinctive feature representation. For the traditional tri-plane, this problem is alleviated by using several tri-planes at different resolutions. The essence of this solution is to reduce the likelihood of overlapped projections by considering different sizes for cells on the feature plane. As a side effect, this solution needs to afford a large number of parameters, which will be proved in Table III. The second case is when two or more primitives are in a line that is perpendicular to a certain feature plane (green, blue, and cyan blocks in Fig. 2). Then their axis-aligned projections on the feature plane are always identical, which cannot be simply solved by enlarging or reducing the cell’s size. Note that two concurrent works dedicated to the static full-head generation, namely PanoHead [20] and SphereHead [21], also report abnormal results caused by this issue when integrating the tri-plane structure in their frameworks. Specifically, they observe the back of the head usually shows the components of the front face (e.g., the eyes appear on the back), the reason for which is points belonging to the front and back of the head are projected to the same location on a certain feature plane, thus causing representation ambiguity. The problem caused by the above two cases is collectively called “feature dilution” of the tri-plane in our paper.

Feature dilution becomes more pronounced in particular head areas with complex geometry, such as regions obscured by lips, hair, and wrinkles, where denser primitives often exist, accompanied by a significant occurrence of overlapping. TILTED [22] aims to achieve a more accurate feature representation of these primitives interpolated on the feature planes by rotating the entire scene simultaneously. While it appears to be effective in static scenarios, shortcomings arise in dynamic scenes. The inherent dynamism of objects disrupts those attempts to address biases in axis-aligned signals by relying on unified scene rotations. Additionally, since rotating the entire object does not change the relative topological structure, it is less effective in mitigating specific feature dilution within overlapped structures.

In this paper, we introduce the GaussianHead, a new method based on deformable 3D Gaussians for faithful head avatar construction and animation. It relies on shape-flexible 3D Gaussians and a compact tri-plane feature container, while a novel Gaussian derivation mechanism allows it to achieve high-quality rendering and competitive model size without relying on a multi-resolution paradigm. Notably, we disentangle the modeling of head geometry and texture attributes. To be concrete, a motion deformation field is first built

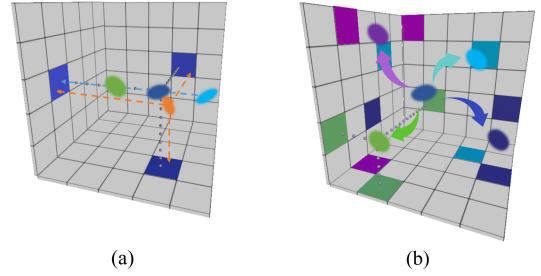


Fig. 2: The adoption of axis-aligned mapping in the tri-plane-formed feature representation is accompanied by a severe problem of “feature dilution”, a visual illustration of that is given in (a). We refer the readers to the third paragraph of the Introduction part for detailed explanations. In contrast, (b) shows our derivation strategy for addressing this problem. Taking the blue Gaussian primitive for example, we first obtain its multiple derivatives through a specific set of learnable transformations and then do feature projection and aggregation. Other 3D Gaussians also undergo the same process.

to fit the whole head shape as well as the dynamic facial movements. In practice, it takes pre-retrieved facial expression coefficients as conditions to transform randomly initialized 3D Gaussians into a posed space. Then we employ a compact data container—parameterized single-resolution tri-plane—to store the appearance information of those Gaussians. To resolve the aforementioned feature dilution problem, we design a novel Gaussian derivation strategy. In short, we generate multiple derivations of each core Gaussian in the posed space using the sets of learnable rotation transformations. By acquiring sub-features from these derived doppelgangers and integrating them, we are able to obtain the precise features of the current Gaussians. In contrast to the multi-resolution regime adopted by the original tri-plane, the Gaussian derivation strategy also reduces the likelihood of feature ambiguity but more effectively and economically. Moreover, a mechanism of inheritance derivation initialization is adopted for newly added Gaussians in the later training phase, improving the convergence speed.

Contributions of this paper are summarized as follows:

- Leveraging anisotropic 3D Gaussian primitives and a parameterized tri-plane with a single resolution to represent the dynamic head avatar compactly.
- The novel strategy of deriving Gaussians effectively alleviates the feature dilution caused by axis-aligned mapping, resulting in a more accurate representation of the texture of complex facial structures.

II. RELATED WORK

A. Scene Primitives in Reconstruction

Whether it is a real-world scenario, the human body, or a head, the foundation of their construction lies in a simple form of scene primitives. Some past approaches rely on implicit primitives. For instance, methods [9], [23], [24] use the signed distance function, which builds objects by tracing points located on the zero-level set of the function

in space. Algorithms [11], [25], [26] leverage the occupancy function to represent 3D surfaces as the continuous decision boundaries of deep neural network classifiers. However, these implicit primitives cannot represent complex head avatars. Methods based on neural radiance fields [27]–[32] store scenes using network weights. However, the necessary manner of constructing a large number of sample points in each ray always leads to significant training overhead. Explicit scene primitives, such as points [33]–[35], can capture sufficiently complex structures. However, due to the fixed shape of points, detailing can only be achieved by continuously refining point radii and increasing point counts during the training process, which introduces significant storage and training cost. Here, we use 3D anisotropic Gaussians [36] as scene primitives. They are deformable in geometric structure, allowing for the representation of intricate details by adjusting their shapes instead of blindly increasing quantity or reducing radii.

B. Sources for Head Portrait Synthesis

The widespread application of head avatars calls for convenient capture modes. Some studies [1]–[3], [37], [38] utilize dense multi-view or binocular vision to record dynamic head avatars in space. Specifically, GaussianHeadAvatar [37] and GaussianAvatars [38] use 3D Gaussians combined with multi-view video to construct finely detailed head avatars. Although this brings better multi-view consistency, the difficulty of popularizing capture devices hinders the rapid adoption of such techniques. Meanwhile, NeRSemble [1] reconstructs head dynamics along the temporal axis, sacrificing cross-subject generalization performance. Some portrait synthesis algorithms start with a single image or a set of images, constructing identity-consistent head avatars through image-to-image transformations. Methods [39]–[42] leverage encoders to encode consistent identities from image sets and regulate outputs by fitting expressions or landmarks from the 3D morphable model. While achieving detailed rendered images, they lack multi-view consistency. Some head avatar methods reconstruct the head by decoupling appearance features [43] or using audio to animate the head avatar [15], [44]–[46]. Other methods track expressions and poses from monocular videos as reconstruction or reenactment conditions [47], [11], [13], [33], [48], [49], achieving increasingly realistic results. Similar to them, our approach also constructs the head avatars based on the monocular video of the target subject.

C. Hybrid Neural Field

Multiple implicit methods [11], [24], [25], [27] have demonstrated that, as the scene’s complexity increases, the learning difficulty for network models also increases. Recently, hybrid neural radiance fields have become popular, which use structured data containers (i.e., tri-plane [50], hexplane [18], [19], and voxel [51]) to store and a decoder to parse the information of scenes. In this manner, the encoding and decoding tasks are undertaken by multiple networks rather than one, reducing the modeling difficulty for each component. However, the commonly employed axis-aligned mappings by these methods will lead to imprecise representation of features. In addition,

their multi-scale design has too many parameters, resulting in huge model sizes. We utilize the tri-plane structure and a decoder to represent a head based on Gaussian primitives in 3D space. The highlight of our approach is the proposed Gaussian derivation strategy and relevant adaptive designs to address the limitations of axis-aligned mapping through dispersing sub-features of each primitive, achieving excellent rendering performance with a small model size. We notice a concurrent work [52] also combines tri-plane with Gaussian splatting but is distinct from us in several aspects: they still query the feature of each Gaussian by projecting it to factored planes along three axes, and they focus on synthesis in static scenarios while ours cares about the dynamic setting.

III. PRELIMINARY OF 3D GAUSSIAN SPLATTING

3D Gaussian Splatting [36] utilizes anisotropic 3D Gaussian primitives to explicitly represent the underlying structure of the scene. The structure of each Gaussian is determined by two parameters defined in world coordinates: position (mean) \mathbf{x} and 3D covariance matrix Σ ,

$$G(\mathbf{x}, \Sigma) = e^{-\frac{1}{2}\mathbf{x}^T \Sigma^{-1} \mathbf{x}}. \quad (1)$$

The intractable covariance matrix can be further decomposed into a scaling matrix \mathbf{S} and a rotation matrix \mathbf{R} , where the correlation between them is $\Sigma = \mathbf{R}\mathbf{S}\mathbf{S}^T\mathbf{R}^T$. For ease of optimization, we optimize a scaling vector \mathbf{s} for \mathbf{S} and a unit quaternion \mathbf{q} for \mathbf{R} in practice. Accordingly, the Gaussian is re-written as $G(\mathbf{x}, \mathbf{q}, \mathbf{s})$. In order to realize rendering, 3D Gaussians need to be projected onto the 2D image plane. Accordingly, the covariance matrix in camera coordinates can be obtained by $\Sigma' = \mathbf{J}\mathbf{W}\Sigma\mathbf{W}^T\mathbf{J}^T$, where \mathbf{W} denotes the view transformation matrix and \mathbf{J} represents the Jacobian matrix approximating the projective transformation [53], [54]. On the other hand, the appearance of every Gaussian is affected by the other two parameters, namely the opacity α and spherical harmonic coefficients Y_{lm} , which are combined with the spherical harmonic basis to represent view-dependent color. For each pixel on the image plane, its color is calculated by blending N ordered 3D Gaussians above it:

$$C = \sum_{i \in N} c_i \alpha_i \prod_{j=1}^{i-1} (1 - \alpha_j), \quad (2)$$

where c_i represents the color of each Gaussian relying on the view direction, and α_i is computed by multiplying the learned opacity of the 3D Gaussian with the probability value of the corresponding 2D Gaussian projected onto the image plane at the current pixel. During the training of those Gaussians, they undergo alternant densification according to the conditions of under- or over-reconstruction and pruning primitives that do not contribute to the rendering results or have overlarge sizes.

IV. APPROACH

Given a monocular video of the target person performing free head and facial movements, the corresponding expression parameters and masks of each frame, and known camera parameters, the proposed GaussianHead is trained on these

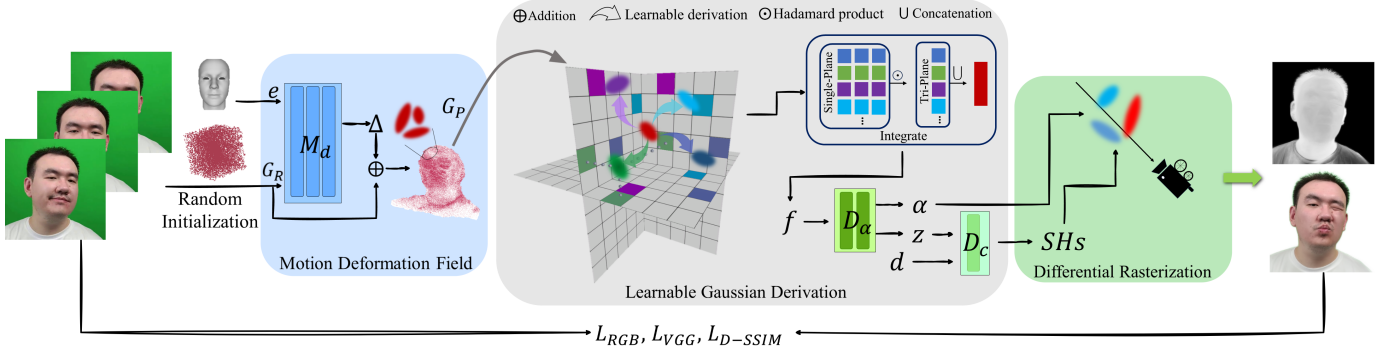


Fig. 3: *Method overview.* GaussianHead uses a set of 3D Gaussians with learnable attributes controlling their shape and appearance to model the subject’s head. A motion deformation field is first set up to represent the dynamic head geometry, which converts structureless Gaussians G_R to structured core ones G_P in a posed space via conditioning on pre-acquired expression parameters e . Next, a single-resolution tri-plane structure of the feature container is leveraged to store appearance-related attributes. Notably, derivation mechanisms through learnable rotations are applied to each core Gaussian, yielding several doppelgangers of it. The integration of sub-features obtained through projection onto the planes from those doppelgangers is taken as the final feature f of the core Gaussian. Two separate tiny MLPs are then employed to decode opacity α and spherical harmonic coefficients (SHs), based on which we generate the final rendering via differential rasterization.

four kinds of input. Our method models the complex head geometry based on anisotropic 3D Gaussians. A single-resolution tri-plane with a learnable derivation strategy is leveraged to encode texture information for those Gaussian primitives. Their integration ensures photorealistic rendering results. In inference, the approach allows high-fidelity reconstruction of the target subject and controllable animation by adjusting expression coefficients and view directions. Fig. 3 illustrates the overall workflow.

A. Motion Deformation Field

The original 3D Gaussian splatting technique was devised to reconstruct static scenes. However, human heads in our dynamic setting exhibit complex motions. Thus, we construct a motion deformation field to obtain variable Gaussians connected with the subject’s head motions, which are changeable within a period. Specifically, it first randomly initializes M Gaussians $G_R = \{G(\mathbf{x}_i, \mathbf{q}_i, \mathbf{s}_i)\}_{i=1}^M$ in the initialized canonical space, each of which is connected with three geometric attributes: position \mathbf{x} , rotation represented by unit quaternion \mathbf{q} , and scaling vector \mathbf{s} . Subsequently, the pre-acquired facial expression parameters e and the positional encoding results of each Gaussian’s spatial coordinate \mathbf{x} are concatenated and then fed into a deformation network M_d with a multi-layer perceptron (MLP) as its implementation. For a certain Gaussian, the deformation network predicts $\Delta_{\mathbf{x}}$, $\Delta_{\mathbf{q}}$, and $\Delta_{\mathbf{s}}$, which are offsets in terms of position, rotation, and scale:

$$(\Delta_{\mathbf{x}}, \Delta_{\mathbf{q}}, \Delta_{\mathbf{s}}) = M_d(\gamma(\mathbf{x}), e), \quad (3)$$

where γ represents conducting position encoding on the mean position of the current 3D Gaussian, generating a high-dimensional sine-cosine sequence [27]. Next, we add the obtained offsets to their initial states, yielding $\hat{\mathbf{x}}_i$, $\hat{\mathbf{q}}_i$, and $\hat{\mathbf{s}}_i$. Relevant updates are called core Gaussians $G_P = \{G(\hat{\mathbf{x}}_i, \hat{\mathbf{q}}_i, \hat{\mathbf{s}}_i)\}_{i=1}^M$ in the posed space.

B. Learnable Gaussian Derivation

1) *How to realize it?:* A single motion deformation MLP is sufficient to express complex head movements, but it struggles to simultaneously represent all fine and intricate facial textures (see Sec. V-G). To enhance the representation capability while using minor consumption, a *single-resolution tri-plane* is employed to encode texture information around the subject’s head. These factorized feature planes \mathbf{P}_{xy} , \mathbf{P}_{xz} , \mathbf{P}_{yz} have an identical size of (H, W, L) , where H and W represent the height and width and L denotes the channel length. Then, we derive K doppelgangers from each core Gaussian by imposing an equivalent number of learnable derivations parameterized by unit quaternion \mathbf{r} on it. In practice, we first generate the scalar and vector parts of the quaternion randomly and then do normalization to ensure its magnitude is 1. Since both the rotation axis and rotation angle are unfixed, the rotated Gaussian (i.e., doppelganger) is also variable in both the orientation and position. Note that K is required to evenly divide L . For every individual doppelganger, it is vertically projected onto three factor planes, generating three individual plane feature vectors by sequentially interpolating L/K channels of factor planes. Three shortened feature vectors from the tri-plane are fused by the Hadamard product, forming the sub-feature of the target doppelganger. Eventually, features from K doppelgangers are concatenated, yielding the final feature representation f for the core Gaussian. Mathematically, that can be expressed as

$$f = \bigcup_{k=1}^K \prod_{j=1}^3 \varphi(\mathbf{P}_j, \mathbf{r}_k(G_P)), \quad (4)$$

where \mathbf{P} represents the parameterized plane with j indexing the xy , xz , and yz factorized planes. The symbol \mathbf{r} denotes the derivation transformation, which is optimized also via a unit quaternion in our practice. In addition, φ indicates the projection of a doppelganger onto a factor plane and subsequent bilinear interpolation, and \bigcup means concatenating short features from multiple doppelgangers.

The unit quaternions controlling the derivation do not have an explicit first-order gradient. Due to manifold constraints, they cannot be straightforwardly optimized in Euclidean space using first-order optimizers. Therefore, we employ the Riemannian ADAM optimizer [55], where updates to unit quaternions at the training step t are induced by an exponential term based on the learning rate α_t and gradient ∇_t in their tangent space:

$$\mathbf{r}_{k,t+1} = \mathbf{r}_{k,t} \text{Exp}(\alpha_t \nabla_t). \quad (5)$$

2) *Why does it work?*: An often overlooked fact is that when the tri-plane with axis-aligned mapping is used for feature representation, the three-dimensional space defined by these orthogonal planes simultaneously couples geometric with appearance attributes. Specifically, any point within this space serves a dual purpose: it not only represents the local shape structure of the object to be modeled but also determines locations on three feature planes for storing the corresponding local appearance information. Regarding the former, in order to achieve local watertightness and completeness of the object’s structure, the point primitives used to represent the target object are typically very dense and occupy only a small portion of the three-dimensional space constructed by the tri-plane. For the latter, when these densely distributed points are projected onto the three feature planes in an axis-aligned manner, the projection regions only cover a small fraction of the entire feature plane, leading to low storage space utilization. Additionally, this results in the first type of feature dilution problem described in the Introduction section (i.e., multiple points being too close together, causing their projections to coincide in the same cells across the three feature grids). Although the multi-resolution mechanism employed by the tri-plane can somewhat alleviate this first type of feature dilution problem, it introduces a large number of parameters. Furthermore, the storage space at each resolution level still remains underutilized, as the projected points only occupy a small subset of the cells on the feature planes. As for the second type of feature dilution problem (i.e., multiple points being located along the same line perpendicular to a feature plane), it cannot be alleviated by this mechanism. Fig. 2(a) visually illustrates the feature dilution issue, aiding comprehension of the preceding discussion.

Our method selects 3D Gaussians as the representation primitives, which, to some extent, can also be viewed as points. The core reason why our proposed “derivation strategy” is effective lies in its decoupling of the two functions of the points in the three-dimensional space corresponding to the tri-plane: one function for representing the object’s geometry and the other for determining the storage location of the appearance features. In practice, we create multiple doppelgangers for each core Gaussian and then use them to determine the storage location for the feature information associated with the current Gaussian point. In other words, we assign the core Gaussian to represent the geometric attributes of the modeled object, while its corresponding doppelgangers are responsible for acquiring the corresponding appearance attributes. This approach effectively avoids the representation ambiguity caused by storing the features of multiple Gaussians

in the same location. An additional benefit of this method is that, theoretically, we can create doppelgangers at any location in the entire three-dimensional space corresponding to the tri-plane, thereby achieving full utilization of the storage region. To gain a deeper understanding of how our design mitigates the feature dilution problem, please refer to Fig. 2(b).

C. Hierarchical Radiance Decoding and Inherited Derivation Initialization

In contrast to recent dynamic scene approaches based on 3D Gaussians [56], [57] that directly set opacity and color as optimizable parameters, we employ two small MLPs to decode the final features into opacity α and spherical harmonic coefficients Y_{lm} :

$$(\alpha, \mathbf{z}) = D_\alpha(\mathbf{f}), \quad (6)$$

$$Y_{lm} = D_c(\mathbf{d}, \mathbf{z}), \quad (7)$$

where \mathbf{z} denotes the intermediate latent code and \mathbf{d} is the view direction. We use 4th-order spherical harmonic coefficients to synthesize view-dependent colors. This design ensures a more precise inference of texture (validated in Sec. V-G). Finally, differentiable rasterization in Eq. 2 is used for rendering.

Recall that the number of Gaussian primitives dynamically increases or decreases during their training process. Given a new Gaussian copied by or split from the original entity, it proceeds to derive multiple doppelgangers via optimizable rotations in our method. Regarding the optimization of rotation parameters, we employ an inheritance initialization strategy, which means initializing them with the same values the parent Gaussian uses. Experiments show that, compared to random or zero initialization, the inheritance strategy increases the training speed by approximately 25%. We describe this setting in more detail and conduct experimental comparisons in Sec. V-F.

D. Training Objectives

We utilize L1 loss L_{RGB} to measure the pixel-wise difference between the ground truth image and its corresponding rendering. The perceptual loss L_{VGG} [58] and D-SSIM loss $L_{\text{D-SSIM}}$ are leveraged to measure the quality loss of the rendered images. Specifically, for the perceptual loss, we use the first four layers of the VGG model [59] to extract feature maps from compared image pairs for subsequent similarity computation. The full objective function as well as its components are given as follows:

$$L = \lambda_1 L_{\text{RGB}} + \lambda_2 L_{\text{VGG}} + \lambda_3 L_{\text{D-SSIM}}, \quad (8)$$

$$L_{\text{RGB}} = \|\mathbf{I} - \mathbf{I}^{\text{GT}}\|_1, \quad (9)$$

$$L_{\text{VGG}} = \|\text{VGG}(\mathbf{I}) - \text{VGG}(\mathbf{I}^{\text{GT}})\|_1, \quad (10)$$

$$L_{\text{D-SSIM}} = 1 - \text{SSIM}(\mathbf{I}, \mathbf{I}^{\text{GT}}), \quad (11)$$

where we empirically set $\lambda_1 = 0.8$, $\lambda_2 = 0.01$, and $\lambda_3 = 0.2$.

V. EXPERIMENTS

A. Datasets and Baselines

All monocular videos for experiments are sourced from public subjects, including real-life and internet recordings. We take the first part of every video clip for models' training, varying between 2000 and 2500 frames. The remaining ones constitute the testing samples. For each subject, we pre-process corresponding videos to get four modality signals: RGB head images with a unified resolution of 512×512 , expression parameters tracked by a 3DMM model [5], camera parameters, and binary masks predicted by MODNet [60]. Regarding the head movement, we follow the practice in [13], [28], which anchors the head in the coordinate system and simulates its pose changes with camera poses.

We compare our approach with six state-of-the-art methods for evaluation purposes. SplattingAvatar [49] binds 3D Gaussian to 3DMM, thus capable of utilizing the excellent rendering quality of 3D Gaussian and the effective motion control manner of 3DMM to construct a head avatar. INSTA [48] is based on volumetric NeRF and reconstructs avatars by building a neural surface on the foundation of 3DMM. PointAvatar [33] is based on explicit points and constructs detailed avatars through iterative refining and upsampling point clouds. NeRFBlendShape [13] constructs a hybrid NeRF and utilizes a multi-resolution hash grid to store facial expression bases. MonoGaussianAvatar [61] models dynamic head avatars by leveraging 3D Gaussian points in combination with a Gaussian deformation field, and introduces a novel insertion-deletion strategy to facilitate improved convergence. GaussianBlendShape [62] represents the head avatar as a linear combination of a base model of neutral expression and a set of expression blendshapes, all of which are represented by learned 3D Gaussians. It also imposes a consistency constraint between the Gaussian blendshapes and the mesh blendshapes, significantly reducing artifacts in the boundary regions of the subject under novel expressions.

B. Implementation Details

We implement GaussianHead with PyTorch, where differentiable 3D Gaussian rasterization is implemented based on CUDA kernels [36]. The initialization included 10K 3D Gaussians. Apart from optimizing the derivative quaternion using Riemannian ADAM [55], all other optimizers are first-order ADAM [63]. Specifically, for the unit quaternion q representing 3D Gaussian rotation, we follow the explicitly first-order gradients as derived in [36] and also optimize it using ADAM. In our experiments, we set the batch size to 1 and train the model on a single RTX 3090, taking approximately 2 hours. After 3000 iterations, we perform densification and pruning on 3D Gaussians every 500 iterations, pruning Gaussians larger than a certain proportion of the scene and removing Gaussians with opacity below the threshold. We set the size threshold for large Gaussians to be greater than 1% of the scene and the opacity threshold to 0.0002. Other details follow the settings in [36].

For the tri-plane structural feature container, we set the size of each plane to $64 \times 64 \times 32$ ($H \times W \times L$). Re-

garding the derivative unit quaternions r , they are treated as trainable parameters, initialized with random numbers in the range $[0, 2^{32}]$, and uniformly distributed on a 3-dimensional hypersphere to obtain unit quaternions with better distribution properties. Their learning rate decays from 1×10^{-3} to 0 at the last iteration.

C. Comparison with State-of-the-art Approaches

Reconstruction. This task is to construct a lifelike avatar of the target person in the reference video and make it perform the same actions. We showcase visual comparison results rendered by our method and baselines in Fig. 4. PointAvatar uses the built-in linear blend skinning (LBS) algorithm of 3DMM to control facial movements. By linearly combining expression coefficients and expression bases, this limited representation method often fails to accommodate extreme expressions. As evidence, please see the snapshots of avatars generated by this approach in Fig. 4, which fail to accurately depict mouth movements. Dynamic results in the supplementary video present a more intuitive demonstration of this particular deficiency. In addition, since the primitives adopted are points with fixed shapes, this approach may yield holes during reconstruction (7th row). SplattingAvatar employs 3DMM mesh as the geometry prior of the human head and makes all Gaussians attached to triangle meshes. With this design, in practice, it realizes animation akin to INSTA, which is based on direct mesh movement rather than LBS techniques. However, a side effect is that it needs to calculate the variation of 3D Gaussian properties using the motion of coarse mesh triangles, which occasionally results in inaccurate modeling of facial expressions. NeRFBlendShape exhibits rendering blur when reconstructing complex surfaces such as lips and eyes, which may be due to the inaccurate density estimation in the modeling of geometric surfaces. INSTA models the head based on a predefined 3DMM geometry, making it struggle to represent the fine structures (e.g., the jewelry in the 3rd and the suspended hair in the 6th row). MonoGaussianAvatar relies on the rough FLAME template and skinning weights and uses the LBS algorithm for motion control, and thus performs relatively poorly in capturing subtle expressions (such as the eye-closing action in the 2nd row).

In contrast, our GaussianHead can accurately render subtle details such as slightly closed eyes and wrinkles. Even if only a few frames show the oral cavity in the training data, we can achieve precise reconstruction (refer to Fig. 12). According to the best of our knowledge, this achievement is hard to obtain for previous head avatar approaches that also train their algorithms on monocular videos.

On the other hand, the error map, as opposed to the RGB image, can reflect the reconstruction accuracy more clearly. In practice, we calculate the L1 distance between the reconstructed images and the corresponding ground truth at the pixel level, the results of which are further mapped into the RGB space to produce the final error maps. Fig. 5 clearly shows that our method achieves better reconstruction accuracy than others. Evaluation results tabulated in Table I quantitatively demonstrate our superiority under three image quality related metrics.

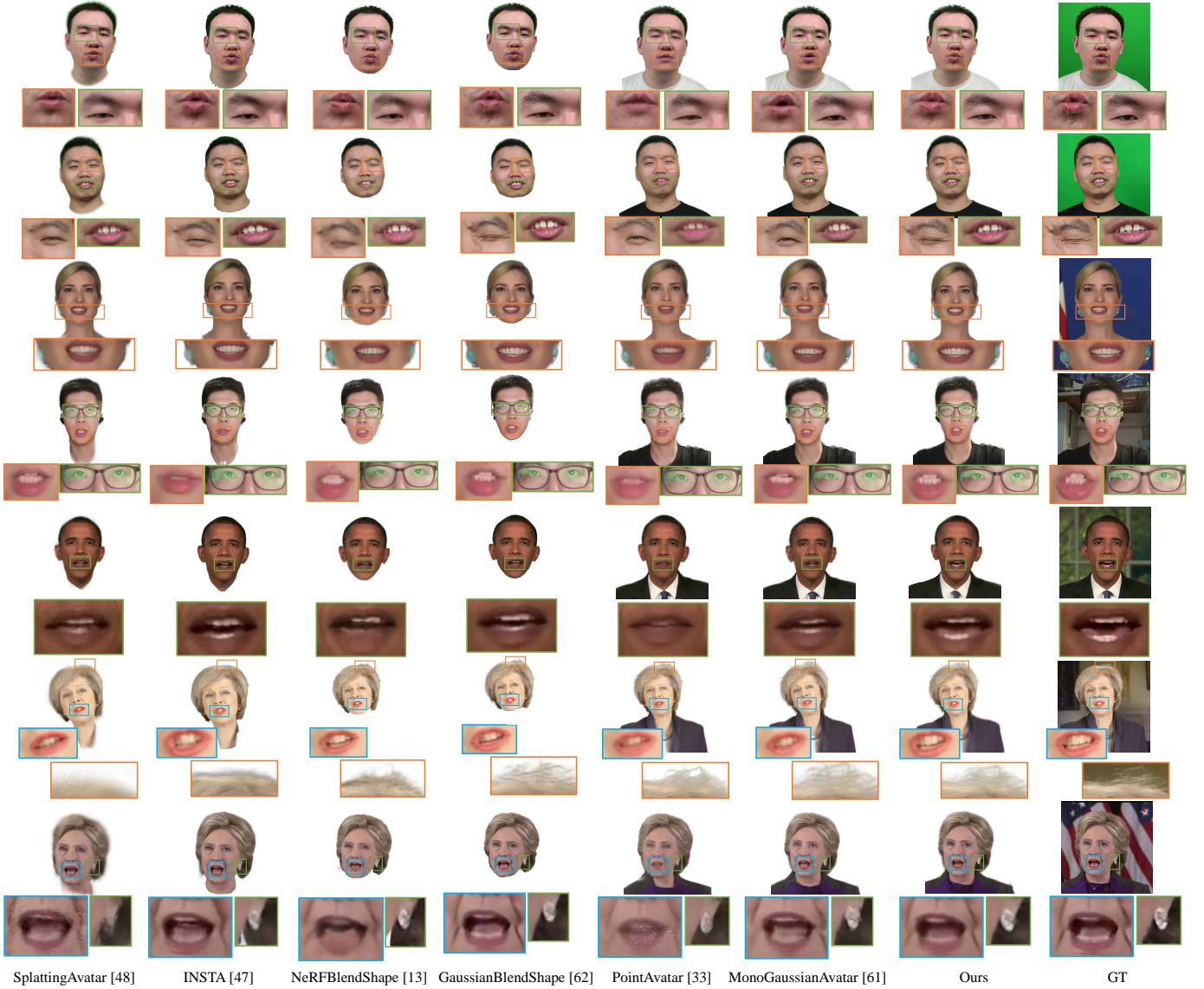


Fig. 4: Qualitative comparisons of the reconstruction task. All competitors are run under the configurations specified by their respective works. Our method achieves superior visual results, particularly in aspects such as wrinkles, teeth, eyebrows, and even reflections on glasses.

Reenactment. This setting is more challenging than the reconstruction task because it aims to transfer the motion patterns of one real subject to the constructed avatar with a different identity. We showcase the reenactment results in Fig. 6. MonoGaussianAvatar, PointAvatar and SplattingAvatar struggle to reproduce even non-subtle and non-extreme expressions. In some frames, significant distortions in poses or expressions are observed. For illustration, in the 1st row of Fig. 6, MonoGaussianAvatar and PointAvatar fails to reproduce the neck’s state accurately. In the second row, SplattingAvatar cannot model the entire face successfully. The biggest problem with INSTA and GaussianBlendShape is the apparent identity discrepancy with the animated avatar where the source and target human objects have significantly different external shapes (e.g., one person has a long face, and the other has a round face). In other words, the avatar and its corresponding real

human object look like belonging to two different persons. For evidence, please see the snapshots by them two in the 2nd and 5th rows of Fig. 6. Note that this issue does not show up in the reconstruction results. NeRFBlendShape performs less satisfactorily in depicting facial details, as all the rendering frames appear over-smoothed. By comparison, the head avatars animated by GaussianHead excel at precisely reproducing the actions and poses of the source subject while depicting facial details and preserving identity consistency simultaneously. Our method still performs well even in imitating extreme facial expressions—for example, the first and third rows of Fig. 6.

Fine comparison with GaussianBlendShape. While GaussianBlendShape demonstrates comparable performance to our method in less challenging scenarios, particularly when subjects are in near-frontal views as presented in Figs. 4 and 6, we conduct further evaluations on them, focusing on more

TABLE I: Quantitative comparisons of reconstruction quality. The six subjects in Fig. 4 are indexed as ID1-ID6 from top to bottom.

Method		ID1			ID2			ID3		
		PSNR \uparrow	SSIM \uparrow	LPIPS \downarrow	PSNR \uparrow	SSIM \uparrow	LPIPS \downarrow	PSNR \uparrow	SSIM \uparrow	LPIPS \downarrow
w/o torso	INSTA [48]	27.41	0.892	0.141	28.43	0.906	0.172	25.26	0.903	0.189
	SplattingAvatar [49]	28.42	0.901	0.119	27.24	0.873	0.181	26.14	0.915	0.186
	NeRFBlendShape [13]	30.93	0.913	0.117	30.12	0.917	0.124	28.92	0.961	0.085
	GaussianBlendShape [62]	32.42	<u>0.922</u>	<u>0.111</u>	31.26	<u>0.938</u>	0.105	<u>29.96</u>	0.936	0.115
	GaussianHead (Ours*)	31.85	0.927	0.098	30.75	0.941	0.108	30.05	0.972	0.061
w/ torso	PointAvatar [33]	26.76	0.861	0.162	23.78	0.803	0.191	24.61	0.794	0.182
	MonoGaussianAvatar [61]	29.13	0.916	0.106	29.07	0.909	0.127	27.45	0.947	0.093
	GaussianHead (Ours)	31.70	0.940	0.091	29.21	0.911	0.119	28.70	0.963	0.066
Method		ID4			ID5			ID6		
		PSNR \uparrow	SSIM \uparrow	LPIPS \downarrow	PSNR \uparrow	SSIM \uparrow	LPIPS \downarrow	PSNR \uparrow	SSIM \uparrow	LPIPS \downarrow
w/o torso	INSTA [48]	29.79	0.931	0.095	26.77	0.791	0.131	27.19	0.876	0.095
	SplattingAvatar [49]	30.28	0.928	0.099	26.78	0.760	0.113	26.25	0.812	0.113
	NeRFBlendShape [13]	30.26	0.952	0.094	27.61	0.837	0.081	27.09	0.916	0.075
	GaussianBlendShape [62]	<u>30.73</u>	<u>0.956</u>	<u>0.082</u>	<u>28.26</u>	<u>0.929</u>	0.159	<u>27.86</u>	0.909	0.124
	GaussianHead (Ours*)	30.97	0.969	0.076	28.73	0.962	0.032	28.52	0.973	0.030
w/ torso	PointAvatar [33]	27.11	0.898	0.142	23.36	0.642	0.154	24.71	0.717	0.185
	MonoGaussianAvatar [61]	<u>30.02</u>	0.921	0.097	<u>27.01</u>	<u>0.841</u>	0.102	<u>27.10</u>	0.899	0.098
	GaussianHead (Ours)	30.06	0.947	0.089	27.65	0.893	0.095	28.31	0.904	0.084

¹ The number with bold typeface means the best result and the underline is the second best.

² For a fair comparison, all image metrics were tested under the condition of no background rendering. To compare with those methods without considering the torso part, we also report our corresponding version by removing the torso, denoted by a superscript symbol “*”.

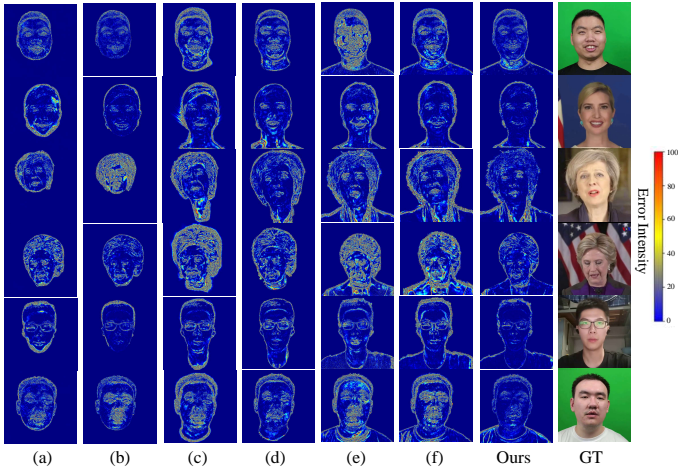


Fig. 5: Error maps for the reconstruction task. We compare with (a) NeRFBlendShape [13], (b) GaussianBlendShape [62], (c) SplattingAvatar [49], (d) INSTA [48], (e) PointAvatar [33] and (f) MonoGaussianAvatar [61]. Note that methods (a-d) only model the head, and (e-f), as well as ours, further include the torso. In each map, brighter areas indicate larger errors.

extreme conditions to assess their performance ceiling rigorously. Representative examples are presented in Fig. 7 and the supplementary video. These results lead to the following observations: 1) GaussianBlendShape exhibits limitations in accurately reconstructing poses where the subject is in profile or near-profile views; 2) In cross-identity reenactment, GaussianBlendShape occasionally produces inaccuracies, including incorrect motion replication, blurred rendering of fine-grained facial details, and color artifacts in the lower face. This is expected, as the reenactment task poses greater challenges than reconstruction. It requires the constructed avatar to replicate the motions and poses of a driving actor with a different

identity while maintaining high image quality in the rendered video frames. Insufficient modeling and disentanglement of the involved facial and head attributes will lead to degraded results; 3) Our GaussianHead demonstrates robust performance in these challenging scenarios, with significant advantages over GaussianBlendShape, especially in the reenactment setup. Furthermore, as highlighted in Table II, our method offers a substantial advantage in model size, being approximately $66\times$ smaller (12MB vs. 800MB) than GaussianBlendShape. This significant reduction in model size makes our approach particularly well-suited for deployment on resource-constrained devices.

More evaluations. Apart from rendering quality, we also conduct evaluations in multiple aspects and record the results in Table II. In brief, our method consumes the minimum GPU memory at inference time, smaller training resource and medium rendering speed with respect to other methods. It is especially noteworthy that we have a much smaller model size ($1/2$ of the second smallest) than competitors. It should be attributed to the derivation mechanism adopted in our framework, which allows the precise encoding of appearance information of 3D Gaussians with a single-resolution tri-plane-formed feature container. More detailed investigation of that will be given in Section V-G.

D. Novel View Synthesis and Depth Estimation

Avatars generated by the proposed GaussianHead exhibit remarkable multi-view consistency, as illustrated in Fig. 8. The results show no artifacts or unrealistic facial expressions. At the same time, our method can also accurately represent details, such as teeth, from novel perspectives. Based on the settings of previous work [57], we additionally present the reconstructed precise depth maps in Fig. 9, from which it can be clearly seen whether there is the presence of artifacts. Our

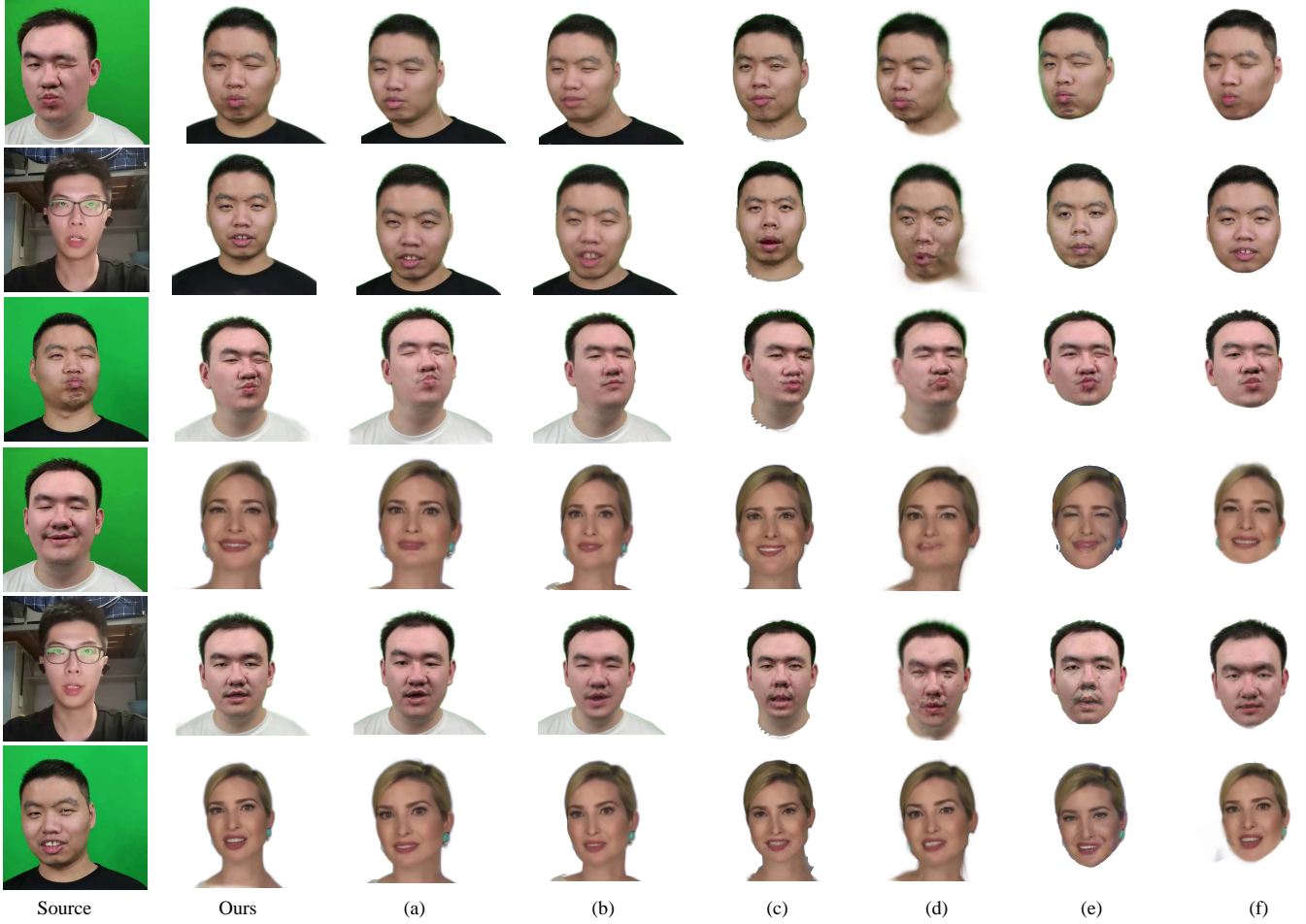


Fig. 6: Qualitative comparisons of the cross-identity reenactment task. Comparison methods include (a) MonoGaussianAvatar [61], (b) PointAvatar [33], (c) INSTA [48], (d) SplattingAvatar [49], (e) GaussianBlendShape [62] and (f) NeRFBlendShape [13]. Our GaussianHead achieves the best reenactment results, even in conveying extreme expressions. For more intuitive comparisons of motion sequences reenacted by these methods, please refer to the supplementary video.

TABLE II: Quantitative comparisons of model size, training cost, and rendering time.

Method	Model Size (MB)↓	Rendering Time (second)↓	Train. Memory (GB)↓	Infer. Memory (GB)↓
SplattingAvatar [49]	84	<u>0.04</u>	11	5
INSTA [48]	<u>60</u>	0.06	16	3.5
NeRFBlendShape [13]	564	0.28	7.5	<u>3</u>
PointAvatar [33]	212	1.5	80	23
GaussianBlendShape [62]	800	<u>0.04</u>	12	4.5
MonoGaussianAvatar [61]	25.7	0.03	10.5	7.5
GaussianHead (ours)	12	0.09	<u>8.5</u>	2.5

¹ The number with bold typeface means the best and the underline is the second best.

² The average rendering time of a single frame is tested on an RTX3090.

method demonstrates excellent depth estimation performance.

E. Number of Doppelgangers

The number of derived doppelgangers (K) significantly influences training time and the final rendering results. We conduct experiments to determine the optimal value by setting it to five different values: 1, 2, 4, 8, and 16 (under the requirement that the count of channels L in each factor

plane, set to 32 in our implementation, is divisible by K). Additionally, we also investigate an adaptive K -scheduler for a more comprehensive evaluation: increasing K with the growing number of Gaussians:

$$K = \frac{L}{2^{t-u}}, u = \left\lceil \frac{n_i}{n_o} \right\rceil, \quad (12)$$

where n_i and n_o are the current and initialized number of Gaussians, $\lceil \cdot \rceil$ denotes the ceiling function, and t is a constant set to 6. Relevant experimental results are shown in Fig. 10. In the context of a fixed value, an excessively large K results in optimization challenges, notably evidenced by a pronounced deceleration in the optimization process at $K = 8$ and 16. Conversely, fewer doppelgangers ($K = 1, 2$) are proven to be inadequate in addressing the issue of feature dilution, leading to a discernible deterioration in PSNR. On the other hand, the incorporation of an adaptive changing scheme (i.e., K -scheduler) does not yield superior outcomes, which should be partially attributed to the predominant occurrence of newly introduced Gaussians in vacant regions. These regions, in contrast to their densely optimized counterparts, have a lower likelihood of encountering feature dilution problems.

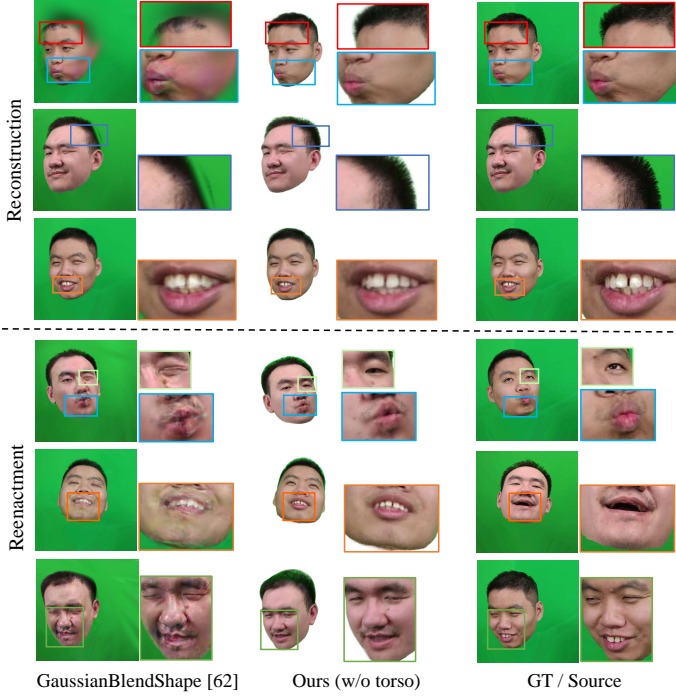


Fig. 7: Comparative results with GaussianBlendShape on challenging cases.

TABLE III: Performance of using different resolution mechanisms for tri-plane and different initialization strategies for Gaussian derivation.

Method	PSNR \uparrow	SSIM \uparrow	LPIPS \downarrow	Model Size (MB) \downarrow	Training Time (hours) \downarrow	Rendering Time (second) \downarrow
M-res	29.89	0.931	0.090	136	~ 3	0.15
R-init	28.85	0.912	0.103	12	~ 2.5	0.09
Z-init	28.42	0.897	0.105	12	~ 2.5	0.09
Ours (S-res, I-init)	29.87	0.938	0.092	12	~ 2	0.09

According to the experimental results, we ultimately choose $K = 4$.

F. Initialization of Derivative Quaternion

In neural radiance fields [22], [27], the number of sampled points in the scene is mostly fixed. However, our GaussianHead undergoes densification or pruning of 3D Gaussians as the iterations progress. For the Gaussians that are clipped out, their quaternions used for controlling derivation are directly deleted. For the newly added ones that split from the parent Gaussian, three initialization schemes for derivative quaternions are studied: randomly initializing from the range $[0, 2^{32}]$ as done at the beginning of training (R-init), zero initialization (Z-init), and inheriting derivative parameters from the parent Gaussian (I-init). The time required for these three schemes to achieve their respective optimal rendering quality is reported in Table III. We observe that the inheriting initialization leads to better rendering results and quicker convergence than its two counterparts. We think these advantages stem from the relatively good starting values provided by the parent Gaussians, reducing the difficulty of parameters optimization.

TABLE IV: Ablation studies on several key components of our GaussianHead.

Method	L1 \downarrow	PSNR \uparrow	SSIM \uparrow	LPIPS \downarrow
w/o tri-plane	0.0014	28.53	0.891	0.144
w/o derivation	0.0013	28.89	0.912	0.115
w/o Δ_s	-	-	-	-
w/o Δ_q	0.0015	28.25	0.901	0.099
w/o Δ_s and Δ_q	-	-	-	-
w/o perceptual loss	0.0017	27.82	0.897	0.151
Direct deform	0.0035	24.55	0.792	0.319
Global rotation	0.0015	28.31	0.901	0.110
Decoded by MLP	0.0023	26.42	0.871	0.195
Ours full	0.0010	29.87	0.938	0.092

¹ The leading dash (-) means the model dose not converge.

² The number with bold typeface means the best and the underline is the second best.

G. Ablation Study

Unless otherwise stated, we conduct ablation experiments on the first three subjects and present the average results.

Parametric tri-plane. Our method employs a parametric tri-plane as the container to store Gaussian appearance information. For comparison, we ablate the parametric tri-plane and directly set the opacity and spherical harmonic coefficients connected with 3D Gaussians as optimizable parameters (“w/o tri-plane”). The ablation results given in Fig. 11 validate the effectiveness of our design. The depth maps yielded by directly optimizing these two radiance parameters lead to numerous redundant Gaussians around the head that will not be removed because their opacity value is above the pre-defined threshold. This inevitably increases training overhead and causes negative perceptual impacts (pay attention to the enlarged local area on the face).

Furthermore, to demonstrate the advantages of parameterized tri-plane in compactly and accurately encoding texture-related knowledge, we replace it with a multi-layer perceptron (“Decoded by MLP”) having a comparable number of parameters. Regarding this variant, our pipeline consists of two MLPs, one for the motion deformation field and the other for decoding texture semantic information from posed Gaussians. When checking its results in Fig. 12, we find that in region not commonly seen in the training videos, such as the oral cavity, it usually renders facial components in colors different from the ground truth. In contrast, our GaussianHead with tri-plane gives precise texture reproduction, even like the lip color and the highlight above earrings. Quantitative results summarized in Table IV align with this observation.

Learnable Gaussian derivation. We make ablation experiments using axis-aligned mappings, following the practice in the traditional tri-plane [18], [50] (“w/o derivation”). Compared to our GaussianHead leveraging the derivation strategy, this variant performs worse in expressing high frequency signals. Additionally, we imitate TILTED [22] by adopting a fixed set of rotations for the entire scene (“Global rotation”) rather than individual primitives. The experimental results support our analysis in Sec. I, global rotation is unsuitable for complex dynamic scenarios.

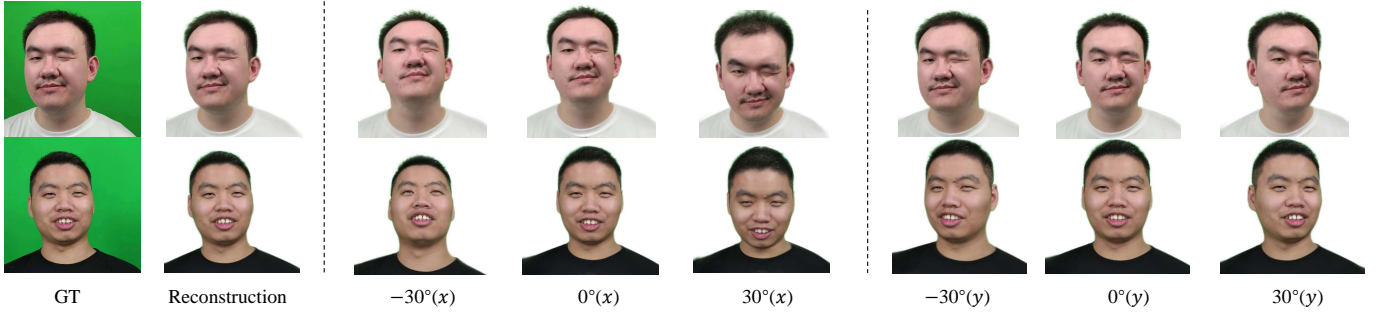


Fig. 8: Novel views rendered by our GaussianHead via rotating the camera viewpoint around the x or y axes. There exists a pronounced consistency in rendering details across these newly synthesized perspectives.

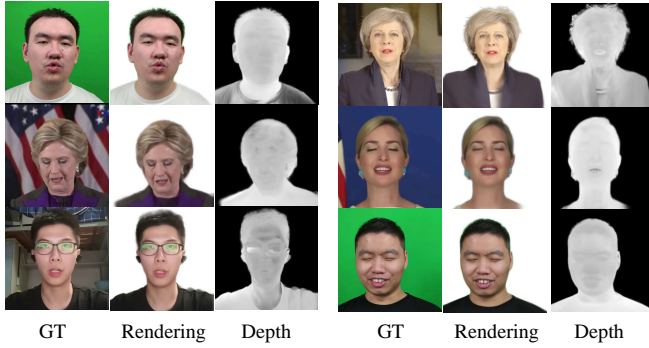


Fig. 9: We reconstruct the ground truth image (left) into a head avatar (center) and simultaneously visualized the depth estimated by GaussianHead (right). Our method obtains accurate depth information.

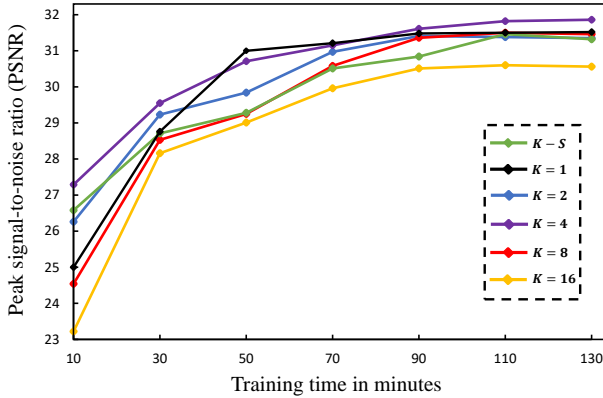


Fig. 10: The performance of taking different numbers of derived doppelgangers K during the training process (“ $K-S$ ” represents the K -scheduler). Optimal performance is achieved when setting K to 4.

Multi-resolution tri-plane. In works like k-planes [18] and hexplane [19], the multi-resolution mechanism of tri-plane is crucial for obtaining high-quality results because of the feature extraction at different scales. However, it also leads to an increase of model size. We investigate the impacts of using this design in our framework (following the settings of previous work [18], we use multiple resolutions of [64, 128, 256, 512]

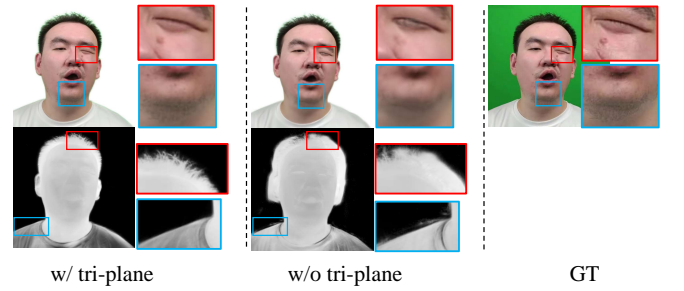


Fig. 11: Visual comparisons of with (w/) or without (w/o) employing the parametric tri-plane structure to store Gaussians appearance information.

in this experiment). Relevant results in Table III show that the induced improvement in rendering quality is almost negligible, whereas the model size grows dramatically. Meanwhile, utilizing a single-resolution tri-plane in our method already achieves comparable visual effects. This should be attributed to the proposed Gaussian derivation strategy, which allows the efficient and precise representation of facial appearance.

Motion deformation field. The motion deformation field is crucial to express dynamic-related expressions. It deserves further exploration on whether directly learning the deformed geometric attributes or predicting their offsets relative to current values. We start with our investigation by separately removing Δ_q (“w/o Δ_q ”), Δ_s (“w/o Δ_s ”) and both of them (“w/o Δ_q and Δ_s ”) to evaluate their influence. This means that during final rendering, we directly take the initialized rotation q , scaling s or both of them as the geometric attributes of deformed 3D Gaussians in the posed space. Experiments show that after removing Δ_s , some Gaussians begin to fluctuate uncontrollably, either becoming too large or too small, leading to the failure of model convergence.

We push forward the ablation by using a MLP to directly predict the properties of 3D Gaussians in the posed space. In this setup, the deformation field predicts all geometric parameters of posed 3D Gaussians, rather than estimating relevant residual values and then adding them to the initials. We report relevant performance (“Direct deform”) in Table IV and Figure 13. The experimental results indicate that, both in terms of quantitative metrics and visual effects, predicting the geometric properties of posed Gaussians directly rather

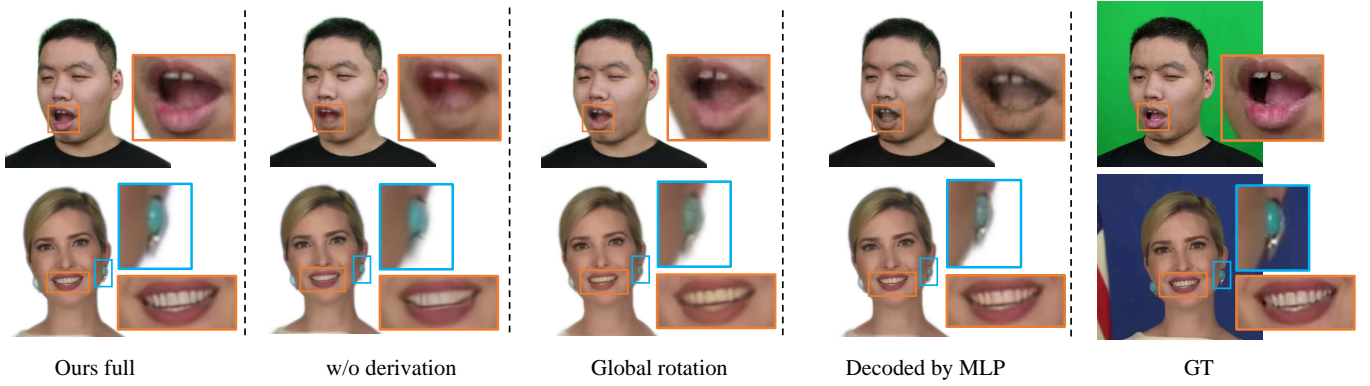


Fig. 12: Qualitative demonstration of partial ablation experiments. The novel Gaussian derivation strategy accurately restores features representing various complex structure regions, enabling the high-fidelity rendering of subtle details even for oral cavity rarely seen in the training data.

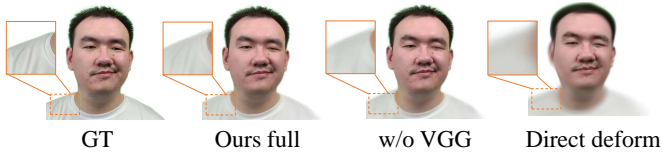


Fig. 13: Visual results without employing perceptual loss and using direct deformation field.

than their residual values yields significantly inferior results. We deduce that direct inference poses many difficulties to the network in specifically distinguishing head regions influenced by dynamic expression parameters, resulting in widespread blurring in areas outside the face.

Perceptual loss. During the training process, our GaussianHead is supervised by minimizing a perceptual loss, actually striving to shorten the distance between the features extracted from two images using a pre-trained VGG [59] model. We observe that employing this loss effectively preserves the consistency in details between the rendered image and its origin reference. By comparison, the removal of it causes a significant decrease in the rendering quality, as evidenced by the results in Fig. 13 and Table IV.



Fig. 14: Failure case. When significant movement occurs in the ground truth (left), the rendered avatar’s torso (middle) will exhibit visible corresponding movement. For clarity, we extract and superimpose their contours (right) for comparison. Compared to the ground truth contours (green), the contours of the rendered avatar (blue) show certain offsets in the torso. Please refer to the supplementary video for the animation.

VI. DISCUSSION

Although our method achieves excellent visual effects, it does not separate the motion of the head and torso. Instead, it still uses camera parameters as rough proxies for pose parameters, which is a common practice in some avatar works (e.g., NeRFBlendShape [13] and INSTA [48]). However, this may result in unnatural shoulder shaking in scenarios with significant motion differences between the head and torso (see Fig. 14). Existing separation methods either utilize semantic masks for independent training of these two parts [15], [44], [45] or explicitly control their motions separately using the LBS algorithm of 3DMM [11], [33]. The former complicates the entire training process, making it unable to achieve end-to-end training and incurring additional training overhead. The latter, while capable of separately controlling the broad-range pose movements of the head and torso, performs poorly in controlling subtle expressions (because it is difficult for 3DMM to represent most complex expressions), as demonstrated by the expression distortion issues in the supplementary video of PointAvatar. Therefore, exploring a practical end-to-end method that achieves separate control of partial structures on the head while effectively expressing subtle facial expressions should be a valuable direction for future work. Some promising solutions include:

- Endowing each Gaussian with a new attribute to reveal which part it models—the head or the torso. Being aware of this, we can construct a deformation field purely responsible for facial dynamics and use the LBS to control the articulated changes in head and torso poses.
- Incorporating a virtual joint approach similar to the one used in [64] to compensate for muscle movements not fully controlled by LBS, thereby addressing the limitations of 3DMM in expression control.

VII. CONCLUSION

In conclusion, this paper introduces GaussianHead, a novel approach leveraging 3D anisotropic Gaussians to construct high-fidelity head avatars and produce reliable animations. Our method presents an effective framework for utilizing

Gaussian primitives to model geometrically variable heads with continuous motions and represent complex textures. With its compact single-resolution tri-plane feature structure and innovative derivation strategy, GaussianHead demonstrates exceptional performance in handling challenging scenarios, such as intricate skin details, voluminous hair, limited training data for oral cavities, and extreme facial expressions, all while maintaining a considerably small model size. We anticipate that GaussianHead will serve as a valuable source of inspiration for the followers.

ACKNOWLEDGMENTS

This work was supported in part by the National Nature Science Foundation of China under Grants 61931012, 62301278, and 62371254; in part by the Science and Technology Development Fund, Macau SAR, under Grants 0141/2023/RIA2 and 0193/2023/RIA3; in part by the Nature Science Foundation of Jiangsu Province of China under Grants BK20230362 and BK20210594; and in part by the Natural Science Research Start-up Foundation of Recruiting Talents of Nanjing University of Posts and Telecommunications under Grants NY222019 and NY221019.

REFERENCES

- [1] T. Kirschstein, S. Qian, S. Giebenhain, T. Walter, and M. Nießner, “Nersemble: Multi-view radiance field reconstruction of human heads,” *arXiv preprint arXiv:2305.03027*, 2023.
- [2] K. Teotia, X. Pan, H. Kim, P. Garrido, M. Elgharib, C. Theobalt *et al.*, “Hq3davatar: High quality controllable 3d head avatar,” *arXiv preprint arXiv:2303.14471*, 2023.
- [3] C. Cao, V. Agrawal, F. De La Torre, L. Chen, J. Saragih, T. Simon, and Y. Sheikh, “Real-time 3d neural facial animation from binocular video,” *ACM Transactions on Graphics*, vol. 40, no. 4, pp. 1–17, 2021.
- [4] V. Blanz and T. Vetter, “A morphable model for the synthesis of 3d faces,” in *Proceedings of the 26th Annual Conference on Computer Graphics and Interactive Techniques*, 1999, p. 187–194.
- [5] T. Gerig, A. Morel-Forster, C. Blumer, B. Egger, M. Luthi, S. Schönborn, and T. Vetter, “Morphable face models—an open framework,” in *Proceedings of the IEEE International Conference on Automatic Face and Gesture Recognition*, 2018, pp. 75–82.
- [6] T. Li, T. Bolkart, M. J. Black, H. Li, and J. Romero, “Learning a model of facial shape and expression from 4d scans,” *ACM Transactions on Graphics*, vol. 36, no. 6, pp. 194–1, 2017.
- [7] L. Ma and Z. Deng, “Real-time hierarchical facial performance capture,” in *Proceedings of the ACM SIGGRAPH Symposium on Interactive 3D Graphics and Games*, 2019, pp. 1–10.
- [8] C. Cao, D. Bradley, K. Zhou, and T. Beeler, “Real-time high-fidelity facial performance capture,” *ACM Transactions on Graphics*, vol. 34, no. 4, pp. 1–9, 2015.
- [9] L. Yariv, Y. Kasten, D. Moran, M. Galun, M. Atzmon, B. Ronen, and Y. Lipman, “Multiview neural surface reconstruction by disentangling geometry and appearance,” in *Proceedings of the Advances in Neural Information Processing Systems*, 2020, pp. 2492–2502.
- [10] L. Yariv, J. Gu, Y. Kasten, and Y. Lipman, “Volume rendering of neural implicit surfaces,” in *Proceedings of the Advances in Neural Information Processing Systems*, 2021, pp. 4805–4815.
- [11] Y. Zheng, V. F. Abrevaya, M. C. Bühler, X. Chen, M. J. Black, and O. Hilliges, “Im avatar: Implicit morphable head avatars from videos,” in *Proceedings of the IEEE/CVF Conference on Computer Vision and Pattern Recognition*, 2022, pp. 13 545–13 555.
- [12] C. Lin, K. Nagano, J. Kautz, E. Chan, U. Iqbal, L. Guibas, G. Wetzstein, and S. Khamis, “Single-shot implicit morphable faces with consistent texture parameterization,” in *ACM SIGGRAPH 2023 Conference Proceedings*, 2023, pp. 1–12.
- [13] X. Gao, C. Zhong, J. Xiang, Y. Hong, Y. Guo, and J. Zhang, “Reconstructing personalized semantic facial nerf models from monocular video,” *ACM Transactions on Graphics*, vol. 41, no. 6, pp. 1–12, 2022.
- [14] Y. Xu, L. Wang, X. Zhao, H. Zhang, and Y. Liu, “Avatarmav: Fast 3d head avatar reconstruction using motion-aware neural voxels,” in *Proceedings of the ACM SIGGRAPH*, 2023, pp. 1–10.
- [15] J. Li, J. Zhang, X. Bai, J. Zhou, and L. Gu, “Efficient region-aware neural radiance fields for high-fidelity talking portrait synthesis,” in *Proceedings of the IEEE/CVF International Conference on Computer Vision*, 2023, pp. 7568–7578.
- [16] Z. Peng, W. Hu, Y. Shi, X. Zhu, X. Zhang, H. Zhao, J. He, H. Liu, and Z. Fan, “Synctalk: The devil is in the synchronization for talking head synthesis,” *arXiv preprint arXiv:2311.17590*, 2023.
- [17] K. Cho, J. Lee, H. Yoon, Y. Hong, J. Ko, S. Ahn, and S. Kim, “GaussianTalker: Real-time talking head synthesis with 3d gaussian splatting,” in *Proceedings of the 32nd ACM International Conference on Multimedia*, 2024, pp. 10985–10994.
- [18] S. Fridovich-Keil, G. Meanti, F. R. Warburg, B. Recht, and A. Kanazawa, “K-planes: Explicit radiance fields in space, time, and appearance,” in *Proceedings of the IEEE/CVF Conference on Computer Vision and Pattern Recognition*, 2023, pp. 12 479–12 488.
- [19] A. Cao and J. Johnson, “Hexplane: A fast representation for dynamic scenes,” in *Proceedings of the IEEE/CVF Conference on Computer Vision and Pattern Recognition*, 2023, pp. 130–141.
- [20] S. An, H. Xu, Y. Shi, G. Song, U. Y. Ogras, and L. Luo, “Panohead: Geometry-aware 3d full-head synthesis in 360deg,” in *Proceedings of the IEEE/CVF conference on computer vision and pattern recognition*, 2023, pp. 20 950–20 959.
- [21] H. Li, C. Chen, T. Shi, Y. Qiu, S. An, G. Chen, and X. Han, “Spherehead: stable 3d full-head synthesis with spherical tri-plane representation,” in *Proceedings of European Conference on Computer Vision*, 2024, pp. 324–341.
- [22] B. Yi, W. Zeng, S. Buchanan, and Y. Ma, “Canonical factors for hybrid neural fields,” in *Proceedings of the IEEE/CVF International Conference on Computer Vision*, 2023, pp. 3414–3426.
- [23] L. Yariv, P. Hedman, C. Reiser, D. Verbin, P. P. Srinivasan, R. Szeliski, J. T. Barron, and B. Mildenhall, “BakedSDF: Meshing neural SDFs for real-time view synthesis,” *arXiv preprint arXiv:2302.14859*, 2023.
- [24] J. J. Park, P. Florence, J. Straub, R. Newcombe, and S. Lovegrove, “Deepsdf: Learning continuous signed distance functions for shape representation,” in *Proceedings of the IEEE/CVF Conference on Computer Vision and Pattern Recognition*, 2019, pp. 165–174.
- [25] L. Mescheder, M. Oechsle, M. Niemeyer, S. Nowozin, and A. Geiger, “Occupancy networks: Learning 3d reconstruction in function space,” in *Proceedings of the IEEE/CVF Conference on Computer Vision and Pattern Recognition*, 2019, pp. 4460–4470.
- [26] S. Peng, M. Niemeyer, L. Mescheder, M. Pollefeys, and A. Geiger, “Convolutional occupancy networks,” in *Proceedings of the European Conference on Computer Vision*, 2020, pp. 523–540.
- [27] B. Mildenhall, P. P. Srinivasan, M. Tancik, J. T. Barron, R. Ramamoorthi, and R. Ng, “Nerf: Representing scenes as neural radiance fields for view synthesis,” *Communications of the ACM*, vol. 65, no. 1, pp. 99–106, 2021.
- [28] G. Gafni, J. Thies, M. Zollhofer, and M. Nießner, “Dynamic neural radiance fields for monocular 4d facial avatar reconstruction,” in *Proceedings of the IEEE/CVF Conference on Computer Vision and Pattern Recognition*, 2021, pp. 8649–8658.
- [29] R. Martin-Brualla, N. Radwan, M. S. Sajjadi, J. T. Barron, A. Dosovitskiy, and D. Duckworth, “Nerf in the wild: Neural radiance fields for unconstrained photo collections,” in *Proceedings of the IEEE/CVF Conference on Computer Vision and Pattern Recognition*, 2021, pp. 7210–7219.
- [30] H. Zhang, F. Li, J. Zhao, C. Tan, D. Shen, Y. Liu, and T. Yu, “Control-free viewpoint video reconstruction based on neural radiance fields and motion graphs,” *IEEE Transactions on Visualization and Computer Graphics*, vol. 29, no. 12, pp. 4891–4905, 2022.
- [31] K. Wang, S. Peng, X. Zhou, J. Yang, and G. Zhang, “Nerfcap: Human performance capture with dynamic neural radiance fields,” *IEEE Transactions on Visualization and Computer Graphics*, vol. 29, no. 12, pp. 5097–5110, 2022.
- [32] L. Song, A. Chen, Z. Li, Z. Chen, L. Chen, J. Yuan, Y. Xu, and A. Geiger, “Nerfplayer: A streamable dynamic scene representation with decomposed neural radiance fields,” *IEEE Transactions on Visualization and Computer Graphics*, vol. 29, no. 5, pp. 2732–2742, 2023.
- [33] Y. Zheng, W. Yifan, G. Wetzstein, M. J. Black, and O. Hilliges, “Pointavatar: Deformable point-based head avatars from videos,” in *Proceedings of the IEEE/CVF Conference on Computer Vision and Pattern Recognition*, 2023, pp. 21 057–21 067.
- [34] Q. Xu, Z. Xu, J. Philip, S. Bi, Z. Shu, K. Sunkavalli, and U. Neumann, “Point-nerf: Point-based neural radiance fields,” in *Proceedings of the*

- IEEE/CVF Conference on Computer Vision and Pattern Recognition*, 2022, pp. 5438–5448.
- [35] A. Mao, Z. Du, J. Hou, Y. Duan, Y.-j. Liu, and Y. He, “Pu-flow: A point cloud upsampling network with normalizing flows,” *IEEE Transactions on Visualization and Computer Graphics*, vol. 29, no. 12, pp. 4964–4977, 2022.
- [36] B. Kerbl, G. Kopanas, T. Leimkühler, and G. Drettakis, “3d gaussian splatting for real-time radiance field rendering,” *ACM Transactions on Graphics*, vol. 42, no. 4, pp. 1–14, 2023.
- [37] Y. Xu, B. Chen, Z. Li, H. Zhang, L. Wang, Z. Zheng, and Y. Liu, “Gaussian head avatar: Ultra high-fidelity head avatar via dynamic gaussians,” *arXiv preprint arXiv:2312.03029*, 2023.
- [38] S. Qian, T. Kirschstein, L. Schoneveld, D. Davoli, S. Giebenhain, and M. Nießner, “Gaussianavatars: Photorealistic head avatars with rigged 3d gaussians,” *arXiv preprint arXiv:2312.02069*, 2023.
- [39] Z. Zhang, Y. Ge, R. Chen, Y. Tai, Y. Yan, J. Yang, C. Wang, J. Li, and F. Huang, “Learning to aggregate and personalize 3d face from in-the-wild photo collection,” in *Proceedings of the IEEE/CVF Conference on Computer Vision and Pattern Recognition*, 2021, pp. 14 214–14 224.
- [40] W. Yu, Y. Fan, Y. Zhang, X. Wang, F. Yin, Y. Bai, Y.-P. Cao, Y. Shan, Y. Wu, Z. Sun *et al.*, “nafa: Nerf-based one-shot facial avatar reconstruction,” in *Proceedings of the ACM SIGGRAPH*, 2023, pp. 1–12.
- [41] Z. Zhang, R. Chen, W. Cao, Y. Tai, and C. Wang, “Learning neural proto-face field for disentangled 3d face modeling in the wild,” in *Proceedings of the IEEE/CVF Conference on Computer Vision and Pattern Recognition*, 2023, pp. 382–393.
- [42] S. Liu and J. Hao, “Generating talking face with controllable eye movements by disentangled blinking feature,” *IEEE Transactions on Visualization and Computer Graphics*, vol. 29, no. 12, pp. 5050–5061, 2022.
- [43] Y. Hong, B. Peng, H. Xiao, L. Liu, and J. Zhang, “Headnerf: A real-time nerf-based parametric head model,” in *Proceedings of the IEEE/CVF Conference on Computer Vision and Pattern Recognition*, 2022, pp. 20 374–20 384.
- [44] Y. Guo, K. Chen, S. Liang, Y. Liu, H. Bao, and J. Zhang, “Ad-nerf: Audio driven neural radiance fields for talking head synthesis,” in *Proceedings of the IEEE/CVF International Conference on Computer Vision*, 2021.
- [45] J. Tang, K. Wang, H. Zhou, X. Chen, D. He, T. Hu, J. Liu, G. Zeng, and J. Wang, “Real-time neural radiance talking portrait synthesis via audio-spatial decomposition,” *arXiv preprint arXiv:2211.12368*, 2022.
- [46] Y. Zhuang, B. Cheng, Y. Cheng, Y. Jin, R. Liu, C. Li, X. Cheng, J. Liao, and J. Lin, “Learn2talk: 3d talking face learns from 2d talking face,” *IEEE Transactions on Visualization and Computer Graphics*, 2024.
- [47] J. Thies, M. Zollhofer, M. Stamminger, C. Theobalt, and M. Nießner, “Face2face: Real-time face capture and reenactment of rgb videos,” in *Proceedings of the IEEE/CVF Conference on Computer Vision and Pattern Recognition*, 2016, pp. 2387–2395.
- [48] W. Zielonka, T. Bolkart, and J. Thies, “Instant volumetric head avatars,” in *Proceedings of the IEEE/CVF Conference on Computer Vision and Pattern Recognition*, 2023, pp. 4574–4584.
- [49] Z. Shao, Z. Wang, Z. Li, D. Wang, X. Lin, Y. Zhang, M. Fan, and Z. Wang, “SplattingAvatar: Realistic Real-Time Human Avatars with Mesh-Embedded Gaussian Splatting,” in *Proceedings of the IEEE/CVF Conference on Computer Vision and Pattern Recognition*, 2024.
- [50] E. R. Chan, C. Z. Lin, M. A. Chan, K. Nagano, B. Pan, S. De Mello, O. Gallo, L. J. Guibas, J. Tremblay, S. Khamis *et al.*, “Efficient geometry-aware 3d generative adversarial networks,” in *Proceedings of the IEEE/CVF Conference on Computer Vision and Pattern Recognition*, 2022, pp. 16 123–16 133.
- [51] T. Müller, A. Evans, C. Schied, and A. Keller, “Instant neural graphics primitives with a multiresolution hash encoding,” *ACM Transactions on Graphics*, vol. 41, no. 4, pp. 1–15, 2022.
- [52] Z.-X. Zou, Z. Yu, Y.-C. Guo, Y. Li, D. Liang, Y.-P. Cao, and S.-H. Zhang, “Triplane meets gaussian splatting: Fast and generalizable single-view 3d reconstruction with transformers,” *arXiv preprint arXiv:2312.09147*, 2023.
- [53] M. Zwicker, H. Pfister, J. Van Baar, and M. Gross, “Ewa splatting,” *IEEE Transactions on Visualization and Computer Graphics*, vol. 8, no. 3, pp. 223–238, 2002.
- [54] V. B. J. Zwicker Matthias, Pfister Hanspeter and G. Markus, “Surface splatting,” in *Proceedings of the Annual Conference on Computer Graphics and Interactive Techniques*, 2001, pp. 371–378.
- [55] G. Bécigneul and O.-E. Ganea, “Riemannian adaptive optimization methods,” *arXiv:1810.00760*, 2018.
- [56] G. Wu, T. Yi, J. Fang, L. Xie, X. Zhang, W. Wei, W. Liu, Q. Tian, and X. Wang, “4d gaussian splatting for real-time dynamic scene rendering,” *arXiv preprint arXiv:2310.08528*, 2023.
- [57] Z. Yang, X. Gao, W. Zhou, S. Jiao, Y. Zhang, and X. Jin, “Deformable 3d gaussians for high-fidelity monocular dynamic scene reconstruction,” *arXiv preprint arXiv:2309.13101*, 2023.
- [58] R. Zhang, P. Isola, A. A. Efros, E. Shechtman, and O. Wang, “The unreasonable effectiveness of deep features as a perceptual metric,” in *Proceedings of the IEEE/CVF Conference on Computer Vision and Pattern Recognition*, 2018, pp. 586–595.
- [59] K. Simonyan and A. Zisserman, “Very deep convolutional networks for large-scale image recognition,” *arXiv:1409.1556*, 2014.
- [60] Z. Ke, J. Sun, K. Li, Q. Yan, and R. W. Lau, “Modnet: Real-time trimap-free portrait matting via objective decomposition,” in *Proceedings of the AAAI Conference on Artificial Intelligence*, vol. 36, no. 1, 2022, pp. 1140–1147.
- [61] Y. Chen, L. Wang, Q. Li, H. Xiao, S. Zhang, H. Yao, and Y. Liu, “Monogaussianavatar: Monocular gaussian point-based head avatar,” in *Proceedings of ACM SIGGRAPH 2024 Conference Papers*, 2024, pp. 1–9.
- [62] S. Ma, Y. Weng, T. Shao, and K. Zhou, “3D gaussian blendshapes for head avatar animation,” in *Proceedings of ACM SIGGRAPH 2024 Conference Papers*, 2024, pp. 1–10.
- [63] D. P. Kingma and J. Ba, “Adam: A method for stochastic optimization,” *arXiv preprint arXiv:1412.6980*, 2014.
- [64] J. Lei, Y. Wang, G. Pavlakos, L. Liu, and K. Daniilidis, “Gart: Gaussian articulated template models,” *arXiv preprint arXiv:2311.16099*, 2023.



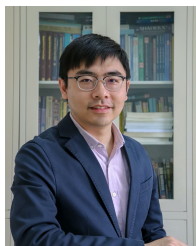
Jie Wang received a BS degree from Hunan University of Chinese Medicine. He is currently working toward the MS degree in Electronic Information at the School of Automation and Artificial Intelligence, Nanjing University of Posts and Telecommunications. His research interests include 3D computer vision and digital humans.



Jiu-Cheng Xie received his PhD degree in Computer and Information Science from the University of Macau in 2022, with a year of study at the Hong Kong Polytechnic University through a doctoral joint training program. He currently holds a lecturer position at the School of Automation and Artificial Intelligence, Nanjing University of Posts and Telecommunications, China. His research interests center on human-centric topics, including analysis, 3D reconstruction, animation, and their interactions with the environment.



Xianyan Li received a BS degree from Yantai University. He is currently working toward the MS degree in Electronic Information at the School of Automation and Artificial Intelligence, Nanjing University of Posts and Telecommunications. His research interests include virtual reality and intelligent robotics.



Feng Xu received the BS degree in physics from Tsinghua University, Beijing, China, in 2007, and the PhD degree in automation from Tsinghua University, Beijing, China, in 2012. He is currently an associate professor with the School of Software, Tsinghua University, China. His research interests include facial animation, performance capture, and 3D reconstruction.



Chi-Man Pun received the B.Sc. and M.Sc. degrees in software engineering from the University of Macau in 1995 and 1998, respectively, and the Ph.D. degree in computer science and engineering from The Chinese University of Hong Kong in 2002. He was the Head of the Department of Computer and Information Science from 2014 to 2019. He is currently a Professor of computer and information science and in charge of the Image Processing and Pattern Recognition Laboratory, Faculty of Science and Technology, University of Macau. He has in-

vestigated many externally funded research projects as a PI, and has authored/coauthored more than 200 refereed papers in many top-tier journals and conferences. His research interests include image processing and pattern recognition; multimedia information security, forensic and privacy; adversarial machine learning and AI security.



Hao Gao is currently a professor with the School of Automation, School of Artificial Intelligence, Nanjing University of Posts and Telecommunications, Nanjing, China. His research interests include artificial intelligence and computer vision, and he has authored or co-authored more than 50 international journal and conference papers. Prof. Gao was the Editorial Member and referee for many international journals.

Supplementary Material - GaussianHead: High-fidelity Head Avatars with Learnable Gaussian Derivation

Jie Wang, Jiu-Cheng Xie, Xianyan Li, Feng Xu, Chi-Man Pun, and Hao Gao

1 NETWORK ARCHITECTURE

Details of the network architecture are shown in Fig. 1. The main parameters to be optimized in our framework include the mean position \mathbf{x} , quaternion-formed rotation \mathbf{q} , and scale s of initial 3D Gaussians, as well as a motion deformation MLP, a single-resolution tri-plane feature container, a radiance decoder MLP, and a set of learnable unit quaternions \mathbf{r} used for deriving each core Gaussian in canonical space.

The deformation network has two inputs: the latent code of \mathbf{x} processed by imposing the positional encoding with a frequency of 10 on it and the tracked expression parameters \mathbf{e} . This module consists of 8 linear layers with a unified width of 256 and skip connections added to the fourth layer. The final linear layer is connected to three parallel heads, each of which is activated using ReLU. They respectively output offsets of the position $\Delta\mathbf{x}$, rotation $\Delta\mathbf{q}$, and scale Δs relative to their initial values.

The parameters of the single-resolution tri-plane are initialized with a uniform distribution in the range $[0.1, 0.5]$. The resolution is set to 64×64 . For the canonical features \mathbf{f} , an opacity network consisting of 3 linear layers with a width of 64 is used to process them. The opacity α is activated by the sigmoid function. The intermediate variables \mathbf{z} are concatenated with the view direction \mathbf{d} and fed into a color network with a depth of 2 and a width of 64. The ReLU function is used for activation purposes, yielding spherical harmonic coefficients Y_{lm} .

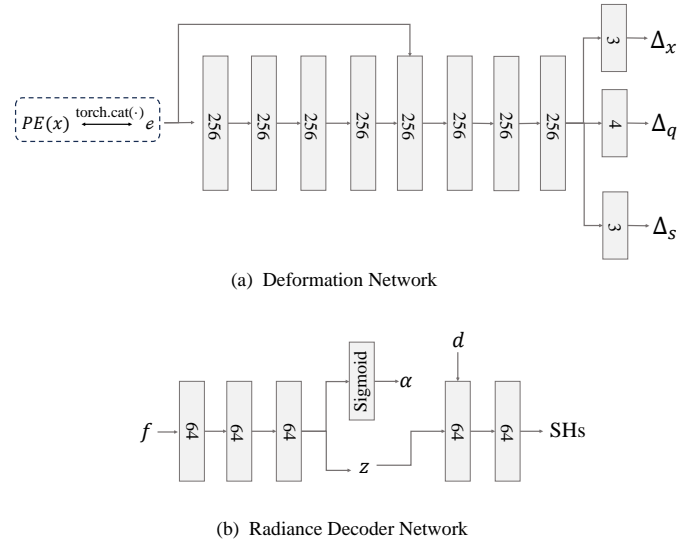


Fig. 1: Diagrams of our network architecture. $PE(\cdot)$ and \mathbf{e} represent position encoding and expression parameters, respectively.

- Jie Wang, Jiu-Cheng Xie, Xianyan Li and Hao Gao are with the School of Automation and the School of Artificial Intelligence, Nanjing University of Posts and Telecommunications, Nanjing, 210023, China. E-mail: chieh.wangs@gmail.com, jiuchengxie@gmail.com, 974598lxy@gmail.com, tsghao@gmail.com.
- Feng Xu is with the School of Software and BNRist, Tsinghua University, Beijing 100084, China. E-mail: xufeng2003@gmail.com.
- Chi-Man Pun is with the Department of Computer and Information Science, University of Macau, Taipa, Macau. E-mail: cmpun@um.edu.mo.
- Jiu-cheng Xie and Hao Gao are the corresponding authors.